PAPER

FGO-MFI: factor graph optimization-based multi-sensor fusion and integration for reliable localization

View the article online for updates and enhancements.

FGO-MFI: factor graph optimization-based multi-sensor fusion and integration for reliable localization

Jiaqi Zhu[1,4] (ORCID)**, Guirong Zhuo**[1,4]**, Xin Xia**[2,*]**, Weisong Wen**[3]**, Lu Xiong**[1]**, Bo Leng**[1] **and Wei Liu**[1]

[1] School of Automotive Studies, Tongji University, Shanghai, 201804, People's Republic of China
[2] Department of Civil and Environmental Engineering of UCLA, Los Angeles, CA 90095, United States of America
[3] Department of Aeronautical and Aviation Engineering, The Hong Kong Polytechnic University, Hong Kong Special Administrative Region of China, People's Republic of China

E-mail: x35xia@g.ucla.edu

CrossMark

Abstract

Reliable and precise information pertaining to the position, velocity, and attitude is essential for automated driving. This paper proposes FGO-MFI, a cost-effective and robust multi-sensor fusion and integration localization framework that utilizes factor graph optimization. Firstly, a tightly coupled Global Navigation Satellite Systems (GNSS)/on-board sensor fusion localization framework is established to estimate vehicle states, including position, velocity, and attitude. To address the large drift rate of the Inertial Measurement Unit (IMU), this study introduces a novel IMU/Dynamics pre-integration method based on the vehicle dynamics model. We establish a two-degree-of-freedom vehicle dynamics model utilizing measurements from the wheel speed sensor and steering wheel angle sensor. The IMU/Dynamics factor is devised through a close integration of the model output and IMU pre-integration, enabling the construction of precise odometry with low-cost on-board sensors. Then, to address the issue of the non-Gaussian distribution of GNSS pseudorange error, this paper employs a Gaussian Mixture Model (GMM) to characterize the pseudorange noise, which is then applied to further sensor fusion. Given the time-varying nature of pseudorange noise, the expectation maximization algorithm is utilized to estimate GMM parameters online, leveraging the pseudorange residuals within a sliding window. Comprehensive experiments, inclusive of challenging scenarios such as urban canyons, tunnels, and wooded areas, have been carried out. They affirm the superior performance of the proposed method. Experiments have shown that our method demonstrates reliable localization across different statuses of GNSS signal, exhibiting a 39.4% improvement in the root mean square error of position error when compared to the state-of-the-art. Additionally, this FGO-MFI is a general sensor data fusion framework and is able to incorporate diverse sensor measurements, for example, from cameras and LiDARs to provide more reliable and accurate localization information.

---

[4] Equal contribution.
[*] Author to whom any correspondence should be addressed.

1. Introduction

Automated driving system (ADS) has boosted the development of intelligent transportation systems, contributing to energy saving, traffic efficiency improvement, and road safety enhancement etc. As a typical cyber-physical system, an ADS comprises complex modules from perception, planning to control. Among these modules, reliable and accurate global localization is an essential component of ADS perception [1]. Addressing the localization challenge requires the integration of various sensors in automated vehicles, including Global Navigation Satellite Systems (GNSS), Inertial Measurement Units (IMUs), cameras [2], LiDAR [3], and radar. GNSS stands out among these for its cost-effectiveness and ability to provide global positioning services. In open sky areas, GNSS can achieve position accuracy within $1 \sim 3$ meters even without real-time kinematic correction (RTK). However, in scenarios such as urban canyons, tunnels, and wooded areas, GNSS signals are prone to interference from multipath effects and non-line-of-sight (NLOS) reception [4]. This interference leads to pseudorange errors at levels reaching tens of meters, significantly undermining GNSS position accuracy. The unpredictability of positioning accuracy [5] is the main obstacle for automated driving applications to fully rely on GNSS, as the inconsistent accuracy is a concern in complex and realistic scenarios.

To mitigate the errors due to multipath and NLOS reception, extensive efforts have been made and they can be divided into two categories: hardware-based and software-based approaches. From the angle of the first one, dual-polarized antennas [6], and antenna arrays [7] are proposed to reduce the interference caused by multipath. This approach will lead to more complex hardware and inevitably increase the cost, which prevents its commercialization in automated vehicles. In addition, combining other available sensors on automated vehicles with GNSS in the form of sensor fusion is a popular trend in academia. This software-based approach can overcome the limitations of GNSS. The fusion of sensors such as LiDAR [8–10] and cameras [11–13] with GNSS shows excellent performance. However, these are sensitive to environment. Vision is significantly affected by light. LiDAR requires enough features and the cost is also a noteworthy issue. In contrast, IMU has been widely used because it is not affected by the environment [14]. However, cost-effective micro-electromechanical systems (MEMS)-IMU suffers from uncertain noise and unstable bias error. Without GNSS correction, long-term integration results in an exponential growth of cumulative errors [15]. Wheel Speed Sensors (WSS), another sensor independent of GNSS and IMU, are also widely installed in vehicles and can be used to improve the integration of GNSS and IMU performance. Existing studies have shown that the integration of GNSS, IMU and WSS promises to provide reliable position for autonomous vehicle navigation [16]. This is because IMU and WSS have the potential to form a reliable and accurate odometry to cover the errors of GNSS. Therefore, the objective of this paper is to achieve accurate and reliable position based on IMU-WSS odometry and by tightly coupling it with GNSS.

For IMU-WSS-based odometry, pure IMU-based or IMU and WSS fusion methods have been explored in literature. Purely IMU-based approaches, also known as inertial navigation systems (INS) [17] or IMU pre-integration [18], are well developed with the high-end IMU sensors. However, when using a MEMS-IMU, the IMU-based odometry error disperses exponentially over time due to unstable biases in acceleration and angular velocity. Therefore, the WSS is commonly combined with IMU to allow for good accuracy over relatively long periods of time, as WSS can provide accurate velocity observation. [17] used the WSS measurement as longitudinal velocity observation for the Kalman filter, which improved the positioning accuracy of the GNSS/INS fusion system. [19] proposed to integrate the wheel speed with the gyroscope measurements to construct a pre-integration and limit the roll and pitch to zero. Based on this, [16] added acceleration measurements to the pre-integration, where the attitude matrix in the wheel speed pre-integration was calculated from the steering wheel angle. Since all of the above methods were based on the assumption of vehicle planar motion, they were unsuitable for land vehicles traveling outdoors on non-flat ground. [20] integrated the angular velocity measurements from the gyroscope with the wheel speed during the pre-integration process without applying the plane motion assumption, achieving better accuracy. However, all of the above methods consider wheel speed measurements as longitudinal speeds. Yet, vehicles possess complex dynamics characteristics, especially affecting the direction of the velocity vector when the vehicle turns [21]. Therefore, vehicle lateral dynamics modeling should be considered. [15, 22] demonstrated that considering the lateral motion of the vehicle could significantly improve the recursive accuracy of IMU/WSS. However, these were GNSS/IMU/WSS loosely coupled framework based on Kalman Filter. When fewer than four GNSS satellites are available, this may fail. Whereas the tightly coupled framework has been shown to achieve good results [23]. On the other hand, compared to filter-based methods, factor graph optimization-based methods have shown superior state estimation ability, especially when using raw GNSS information in a tightly coupled framework under challenging GNSS signal conditions [24]. Therefore, it is essential to explore the high-precision integration of on-board information in a tightly coupled framework based on factor graph optimization. [21, 25] have shown excellent localization performance by combining vehicle dynamics-enhanced pre-integration with LiDAR and vision, respectively. This motivates us to explore combining it with pseudorange information to compensate for the shortcomings of existing pseudorange, IMU, and WSS fusion methods [26] which ignored vehicle dynamic characteristics. As far as our knowledge extends, the literature has yet to involve the tight integration of IMU and vehicle dynamics with raw GNSS within factor graph optimization.

On the other hand, it is worth noting that uncertainty errors in GNSS may lead to performance degradation of fusion-based localization algorithms under the challenging scenarios of GNSS. Where, uncertainty errors often include outliers, Gaussian distributed noise and non-Gaussian

distributed noise. In [10], the Huber loss function [27] was applied to mitigate the influence of GNSS outliers and achieved a certain effectiveness. The algorithm is essentially a classification method, and its performance depends on the hyperparameters trained assuming the noise satisfies a Gaussian distribution. Existing research has shown that non-Gaussian noise introduced by multipath effects and NLOS reception leads to noise model of GNSS would not fit a Gaussian distribution [26]. To address this issue, [28] theoretically analyzed Gaussian mixture models (GMM) by simulating non-Gaussian noise. [29] implemented GMM in the form of least square estimation called sum-mixture. These works demonstrated good potential of GMM in handling non-Gaussian noise problems. [30, 31] applied GMM to GNSS position and GNSS pseudorange noise modeling, and achieved excellent performance, respectively. [26] further improved the accuracy of pseudorange-based GNSS positioning by adaptively estimating the parameters of the noise model through alternating factor graph optimization and expectation-maximization (EM) methods during the optimization process. The good performance of this method in dealing with non-Gaussian noise problems inspires us to apply it to the pseudorange noise modeling in the factor-graph-based fusion framework. However, the accuracy of the noise parameter estimation method depends heavily on a good initial guess of the estimated state, and the existing methods still have shortcomings in this respect.

In this paper, we present a cost-effective and reliable localization framework based on multi-sensor fusion using a factor graph to estimate vehicle states, including position, velocity, and attitude. We propose a novel integrated IMU/Dynamics factors based on combining the 2D vehicle dynamic model with the 3D kinematic model. In addition, we take into account the time-varying characteristics of pseudorange noise to improve the reliability of positioning. Specifically, we propose the pre-integration based on the vehicle dynamic model. By tightly coupling dynamic pre-integration with IMU pre-integration into a united constraint, we build accurate odometry using low-cost onboard sensors. Different from the traditional assumptions of vehicle planar motion, our approach takes into account the 6-DoF motion of the vehicle and the dynamics characteristics of the vehicle, which lead to more accurate relative constraints. Furthermore, we involve pseudorange measurements of GNSS to the factor graph and then perform nonlinear optimization based on a sliding window with partial marginalization to estimate vehicle states. However, the time-varying and even non-Gaussian characteristics of pseudorange noise present challenges in ensuring fusion accuracy. Inspired by [26], we adopt GMM to model the noise of pseudorange measurements. By utilizing the pseudorange residuals within the sliding window, we employ the EM algorithm for online estimation of the GMM parameters. These estimated parameters are then applied in the factor graph optimization. Benefiting from the accurate odometry we built earlier, the estimation accuracy of the noise parameters of the pseudorange is effectively improved. To summarize, the main contributions of this paper are:

- We propose a novel integrated IMU/Dynamics factors based on combining the 2D vehicle dynamic model with the 3D kinematic model. We achieve an accurate odometry using cost-effective onboard sensors (IMU, WSS, and steering wheel angle sensors) by tightly coupling the vehicle dynamics pre-integration with the IMU pre-integration into a common constraint. This integration supports more accurate relative constraints and has the advantage that accuracy is not affected by the environment. In particular, the dynamics pre-integration is constructed by combining the attitude pre-integration of the IMU with the velocity estimation based on the vehicle dynamics model. Compared with the traditional assumptions of vehicle planar motion, our method incorporates the angular velocity obtained from the IMU gyroscope, which considers the three-dimensional attitude angles of the vehicle. In addition, differing from the traditional method, the dynamics characteristics of the vehicle are also taken into account. This allows to obtain a more accurate dynamics pre-integration.

- We propose a multi-sensor adaptive fusion framework based on factor graph. In this framework, our proposed IMU/dynamics factor provides accurate relative constraints, which is tightly integrated with the raw GNSS measurement for precise and reliable vehicle localization. In addition, to address the challenges posed by the time-varying and non-Gaussian characteristics of pseudorange noise in multi-sensor fusion, we incorporate an online estimation of the pseudorange measurement noise model into factor graph optimization, model using GMM. The parameters of the GMM are estimated online from the pseudorange residuals using the EM algorithm. In particular, the pseudorange residuals are calculated based on the state prediction of the IMU/Dynamics factor. As the IMU/Dynamics factor we construct is accurate and environmentally independent, the accuracy of GMM parameter estimation will be further improved, thus effectively mitigating the impact of GNSS outliers on multi-sensor fusion. Moreover, the framework can be easily extended to adaptive fusion with other sensors such as cameras and LiDAR.

The remainder of the paper is organized as follows: section 2 describes the overall structure of the proposed approach. The cost-effective odometry using onboard sensors is then introduced in section 3. Section 4 details the framework for multi-sensor fusion using factor graph, and the online estimation of the noise model for pseudorange. Section 5 provides the experimental validation of the proposed algorithm and discussion. Finally, a summary and future work are concluded in section 6.

2. System overview

The overview of the proposed localization algorithm is shown in figure 1. The algorithm takes inputs from multi-sensor including GNSS receiver, low-cost MEMS IMU, WSS,
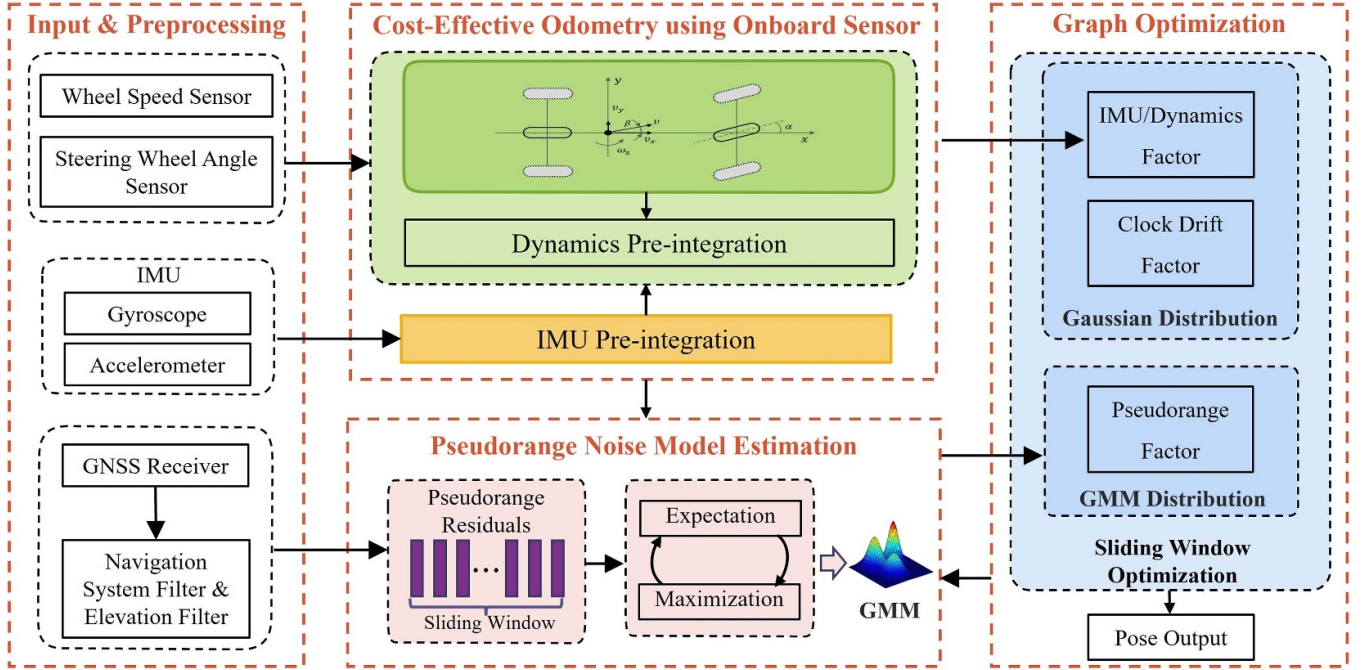
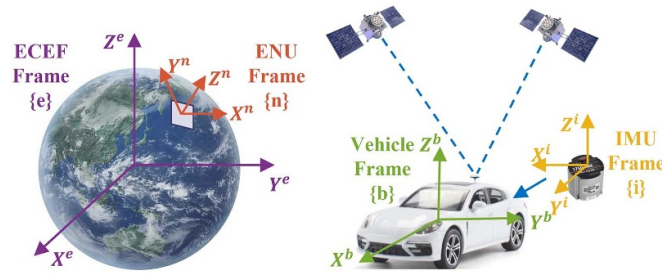**Figure 1.** Overall structure of the proposed localization algorithm.

Figure 2. Illustration of the body$(\cdot)^b$, IMU$(\cdot)^i$, ECEF$(\cdot)^e$, and ENU$(\cdot)^n$ frames.

and steering wheel angle sensor. Firstly, the IMU measurements are used to construct an IMU pre-integration. To improve the accuracy of the vehicle dynamics constraints, an improved dynamics pre-integration is formed by combining a 2D dynamic vehicle model and a 3D kinematic model based on the IMU attitude pre-integration. By integrating the dynamics pre-integration with IMU pre-integration, we construct the IMU/Dynamics factor based on low-cost onboard sensors, which can provide a more accurate relative constraint. Subsequently, when the GNSS measurements become available, necessary preprocessing steps are applied. Only measurements from the GPS navigation satellite system are utilized, while observations from other navigation satellite systems such as Beidou are filtered out. Additionally, low-elevation and unhealthy satellites, which are prone to errors, are excluded. Once the preprocessing phase is completed, the factor graph is expanded to include the IMU/Dynamics factor, clock drift factor and pseudorange factor. In order to alleviate the problem of reduced positioning accuracy caused by time-varying

or even non-Gaussian characteristics of pseudorange noise, the noise parameters of pseudorange factor should be estimated before carrying out the optimization. Next, the pseudorange residuals within a sliding window are calculated based on the estimated states. The residuals are then used as input for the EM algorithm to estimate the noise model for pseudorange online, which is modeled using GMM. Finally, the estimated noise model parameters are fed back to the factor graph optimization for modeling pseudorange factor and the localization solution are obtained by solving the factor graph.

2.1. Frames

As shown in figure 2, the coordinate systems mentioned in this paper are as follows:

1) Body frame$(\cdot)^b$: it is a Cartesian coordinate system fixed to the center of mass of vehicle. All wheel speed measurements are acquired within this frame of reference.

2) IMU frame$(\cdot)^i$: it is a Cartesian coordinate system fixed to the inertial sensors. The IMU is installed at the center of the rear axle of the vehicle, which is aligned with the body frame$(\cdot)^b$ axes as much as possible. Consequently, we do not differentiate between the body frame$(\cdot)^b$ and the IMU frame$(\cdot)^i$.

3) Earth-centered, Earth-fixed (ECEF) frame$(\cdot)^e$: it is a Cartesian coordinate system fixed with respect to the Earth and rotates along with it. In this paper, we use the WGS84 realization of the ECEF frame$(\cdot)^e$. The position information of the satellites is represented in the ECEF frame$(\cdot)^e$.

4) ENU frame$(\cdot)^n$: it is a widely used navigation framework fixed to the carrier. It is aligned with the geodetic axes of East-North-Up. The proposed vehicle localization scheme is developed within this coordinate system.

2.2. Notation

In this paper, we use $\mathbf{R}_n^b$ to denote the rotation from frame$(\cdot)^n$ to frame$(\cdot)^b$. The corresponding Hamilton quaternion $\mathbf{q}_n^b$ is also used, with $\otimes$ representing its multiplication operation. We utilize subscripts to denote the frame corresponding to a particular moment in time. For example, $\mathbf{q}_{b_{k+1}}^{b_k}$ stands for the rotation in terms of quaternion from the frame$(\cdot)^b$ at time t_{k+1} to the frame$(\cdot)^b$ at time t_k.

3. Cost-effective odometry using onboard sensors

The introduction of pre-integration theory avoids the repeated integration of measurements in factor graph optimization, which has the advantage of efficiency. Therefore, more attention has been paid to the pre-integration of IMU measurements or wheel speed measurements to construct relative constraints. However, most WSS-based pre-integration methods are with the assumption of vehicle planar motion. And these ignore the vehicle dynamic characteristic and may lead to reduced accuracy for land vehicles. Therefore, we propose an integrated IMU/Dynamics constraint on the basis of the 2D vehicle dynamic model with the 3D kinematic model, which can construct an accurate odometry with low-cost onboard sensors.

3.1. IMU Pre-integration

We use the methods in VINS-Mono [18] to pre-integrate IMU measurements. Based on acceleration and angular velocity measurements in time interval $[t_k, t_{k+1}]$, the pre-integration terms of position, velocity, and rotation in continuous-time form are

$$
\begin{aligned}
\boldsymbol{\alpha}_{b_{k+1}}^{b_k} &= \iint_{t\in[t_k,t_{k+1}]}\left(\mathbf{R}_{b_t}^{b_k}\left(\mathbf{a}_t - \mathbf{b}_{a_t}\right)\right)\mathrm{d}t^2 \\
\boldsymbol{\beta}_{b_{k+1}}^{b_k} &= \int_{t\in[t_k,t_{k+1}]}\left(\mathbf{R}_{b_t}^{b_k}\left(\mathbf{a}_t - \mathbf{b}_{a_t}\right)\right)\mathrm{d}t \\
\boldsymbol{\gamma}_{b_{k+1}}^{b_k} &= \int_{t\in[t_k,t_{k+1}]}\frac{1}{2}\boldsymbol{\Omega}\left(\boldsymbol{\omega}_t - \mathbf{b}_{\omega_t}\right)\boldsymbol{\gamma}_{b_t}^{b_k}\mathrm{d}t
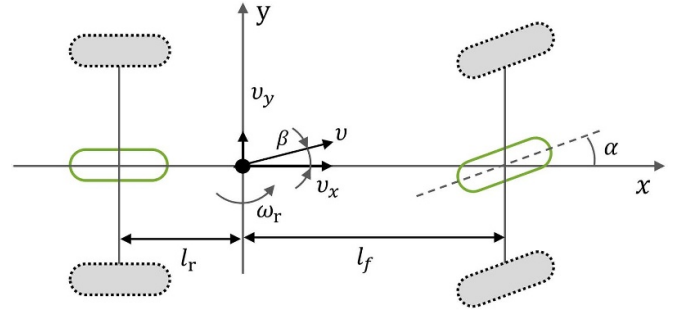\end{aligned}
\tag{1}
$$

Figure 3. The 2-DOF vehicle dynamics model. l_f and l_r represent the distance from the center of mass to the front and rear axles. α is the angle of the front wheel. **v** presents the velocity of vehicle, v_x and v_y are its components along the coordinate axis. The yaw velocity is represented by ω_r, and β is the slip angle.

where

$$
\boldsymbol{\Omega}(\boldsymbol{\omega}) \triangleq \begin{bmatrix} -\lfloor\boldsymbol{\omega}\rfloor_\times & \boldsymbol{\omega} \\ -\boldsymbol{\omega}^T & 0 \end{bmatrix}
$$

$$
\lfloor\boldsymbol{\omega}\rfloor_\times = \begin{bmatrix} 0 & -\omega_z & \omega_y \\ \omega_z & 0 & -\omega_x \\ -\omega_y & \omega_x & 0 \end{bmatrix}
$$

where $\boldsymbol{\alpha}_{b_{k+1}}^{b_k}$, $\boldsymbol{\beta}_{b_{k+1}}^{b_k}$, and $\boldsymbol{\gamma}_{b_{k+1}}^{b_k}$ represent the position, velocity, and rotation pre-integration terms from b_{k+1} to b_k, respectively. $\mathbf{R}_{b_t}^{b_k}$ equals to $\mathbf{R}(\gamma_{b_t}^{b_k})$, which means the rotation matrix form of the $\gamma_{b_t}^{b_k}$. $\mathbf{a}_t$ and $\boldsymbol{\omega}_t$ denote the outputs of IMU at instant t. $\mathbf{b}_{a_t}$ and $\mathbf{b}_{\omega_t}$ represent the accelerometer bias and the gyroscope bias, respectively.

3.2. Dynamics Pre-integration

Odometry methods based on the WSS typically consider the speed observation as the longitudinal speed in the vehicle frame [21]. However, vehicles exhibit complex dynamic characteristics, and particularly, the direction of the velocity is affected when the vehicle is turning. Hence, it is necessary to consider the lateral dynamics model of the vehicle. In normal driving conditions, the vehicle model is usually simplified to a 2D vehicle dynamics model to describe vehicle lateral motion [15] (shown in figure 3). The equation of this model is as follows

$$
\begin{cases}
(k_f + k_r)\beta + \frac{1}{v_x}(l_f k_f - l_r k_r)\omega_r - k_f\alpha = m(\dot{v}_y + v_x\omega_r) \\
(l_f k_f - l_r k_r)\beta + \frac{1}{v_x}\left(l_f^2 k_f + l_r^2 k_r\right)\omega_r - l_f k_f\alpha = I_z\dot{\omega}_r
\end{cases}
\tag{2}
$$

where k_f and k_r represent the lateral stiffness of the front and rear axles. I_z is the moment of inertia, m is the vehicle mass.

As the vehicle makes steady-state steering motion, $\dot{v}_y = 0$, $\dot{\omega}_r = 0$. The slip angle β can be formulated as

$$
\beta_t = \frac{1 + \frac{m}{2l}\frac{l_f}{l_r k_r}v_t^2}{1 - Kv_t^2}\frac{l_r}{l}\alpha_t
\tag{3}
$$

where the coefficient of stability $K = \frac{m}{l}\left(\frac{l_f}{k_r} - \frac{l_r}{k_f}\right)$, $l = l_f + l_r$. v_t and δ_t are the measurements of WSS and steering wheel angle

sensor, respectively. According to the front wheel and steering wheel transmission ratio i, we can obtain the angle of the front wheel by $\alpha_t = \delta_t / i$. The velocity $\hat{\mathbf{v}}_t$ in body frame $(\cdot)^b$ is given as

$$\hat{\mathbf{v}}_t = \begin{bmatrix} v_t \cos \beta_t & v_t \sin \beta_t & 0 \end{bmatrix}^T. \tag{4}$$

By using velocity measurements based on vehicle dynamics model in time interval $[t_k, t_{k+1}]$, we follow the continuous-time quaternion-based derivation as [18] to construct the dynamic update equations of position in ENU frame,

$$\mathbf{p}_{b_{k+1}}^n = \mathbf{p}_{b_k}^n + \int_{t \in [t_k, t_{k+1}]} \left(\mathbf{R}_{b_t}^n \hat{\mathbf{v}}_t \right) dt. \tag{5}$$

To isolate the states so that only pre-integrate the parts related to $\hat{\mathbf{v}}_t$, we convert to body frame. In time interval $[t_k, t_{k+1}]$, the dynamics pre-integration expression in continuous-time as

$$\boldsymbol{\eta}_{b_{k+1}}^{b_k} = \int_{t \in [t_k, t_{k+1}]} \left(\mathbf{R}_{b_t}^{b_k} \hat{\mathbf{v}}_t \right) dt \tag{6}$$

where $\boldsymbol{\eta}_{b_{k+1}}^{b_k}$ is the dynamics pre-integration terms of position. $\mathbf{R}_{b_t}^{b_k}$ is obtained from IMU rotation pre-integration.

3.3. IMU/Dynamics pre-integration

After completing the above two pre-integration, we can get the total IMU/Dynamics pre-integration measurements in time interval $[t_k, t_{k+1}]$ as

$$\boldsymbol{\alpha}_{b_{k+1}}^{b_k} = \iint_{t \in [t_k, t_{k+1}]} \left(\mathbf{R}_{b_t}^{b_k} \left(\mathbf{a}_t - \mathbf{b}_{a_t} \right) \right) dt^2$$

$$\boldsymbol{\beta}_{b_{k+1}}^{b_k} = \int_{t \in [t_k, t_{k+1}]} \left(\mathbf{R}_{b_t}^{b_k} \left(\mathbf{a}_t - \mathbf{b}_{a_t} \right) \right) dt$$

$$\boldsymbol{\gamma}_{b_{k+1}}^{b_k} = \int_{t \in [t_k, t_{k+1}]} \frac{1}{2} \boldsymbol{\Omega} \left(\boldsymbol{\omega}_t - \mathbf{b}_{\omega_t} \right) \boldsymbol{\gamma}_{b_t}^{b_k} dt$$

$$\boldsymbol{\eta}_{b_{k+1}}^{b_k} = \int_{t \in [t_k, t_{k+1}]} \left(\mathbf{R}_{b_t}^{b_k} \hat{\mathbf{v}}_t \right) dt. \tag{7}$$

Note that the equation (7) is not considering the noise. In order to compute the Jacobian matrix and covariance matrix of IMU/Dynamics residuals in the optimization period, we introduce noise and derive the discrete form of the error state kinematics based on median integral. Considering two moments t_τ and $t_{\tau+1}$ in time interval $[t_k, t_{k+1}]$, the time interval between these two moments is denoted as Δt,

$$\begin{bmatrix} \delta\boldsymbol{\alpha}_{b_{\tau+1}}^{b_k} \\ \delta\boldsymbol{\beta}_{b_{\tau+1}}^{b_k} \\ \delta\boldsymbol{\theta}_{b_{\tau+1}}^{b_k} \\ \delta\mathbf{b}_{a_{\tau+1}} \\ \delta\mathbf{b}_{\omega_{\tau+1}} \\ \delta\boldsymbol{\eta}_{b_{\tau+1}}^{b_k} \end{bmatrix} = (\mathbf{I} + \mathbf{F}_\tau \Delta t) \begin{bmatrix} \delta\boldsymbol{\alpha}_{b_\tau}^{b_k} \\ \delta\boldsymbol{\beta}_{b_\tau}^{b_k} \\ \delta\boldsymbol{\theta}_{b_\tau}^{b_k} \\ \delta\mathbf{b}_{a_\tau} \\ \delta\mathbf{b}_{\omega_\tau} \\ \delta\boldsymbol{\eta}_{b_\tau}^{b_k} \end{bmatrix} + \mathbf{G}_\tau \begin{bmatrix} \mathbf{n}_a \\ \mathbf{n}_\omega \\ \mathbf{n}_{b_a} \\ \mathbf{n}_{b_\omega} \\ \mathbf{n}_v \end{bmatrix} \Delta t$$

$$\mathbf{F}_\tau = \begin{bmatrix} 0 & \mathbf{I} & 0 & 0 & 0 & 0 \\ 0 & 0 & -\mathbf{R}\left(\gamma_{b_\tau}^{b_k}\right) \lfloor \mathbf{a}_\tau - \mathbf{b}_{a_\tau} \rfloor_\times & -\mathbf{R}\left(\gamma_{b_\tau}^{b_k}\right) & 0 & 0 \\ 0 & 0 & \lfloor \boldsymbol{\omega}_\tau - \mathbf{b}_{\omega_\tau} \rfloor_\times & 0 & -\mathbf{I} & 0 \\ 0 & 0 & 0 & 0 & 0 & 0 \\ 0 & 0 & 0 & 0 & 0 & 0 \\ 0 & 0 & -\mathbf{R}\left(\gamma_{b_\tau}^{b_k}\right) & 0 & -\mathbf{I} & 0 \end{bmatrix}$$

$$\mathbf{G}_\tau = \begin{bmatrix} 0 & 0 & 0 & 0 & 0 \\ -\mathbf{R}\left(\gamma_{b_\tau}^{b_k}\right) & 0 & 0 & 0 & 0 \\ 0 & -\mathbf{I} & 0 & 0 & 0 \\ 0 & 0 & \mathbf{I} & 0 & 0 \\ 0 & 0 & 0 & \mathbf{I} & 0 \\ 0 & 0 & 0 & 0 & -\mathbf{R}\left(\gamma_{b_\tau}^{b_k}\right) \end{bmatrix}. \tag{8}$$

Based on the linear model subjected to the Gaussian distribution, we can obtain the covariance matrix transfer equation of pre-integrated measurements as

$$\mathbf{P}_{b_{\tau+1}}^{b_k} = (\mathbf{I} + \mathbf{F}_\tau \Delta t) \, \mathbf{P}_{b_\tau}^{b_k} \, (\mathbf{I} + \mathbf{F}_\tau \Delta t)^T + (\mathbf{G}_\tau \Delta t) \, \mathbf{Q} \, (\mathbf{G}_\tau \Delta t)^T \tag{9}$$

where $\mathbf{Q} = \text{diag}\left(\mathbf{n}_a, \mathbf{n}_\omega, \mathbf{n}_{b_a}, \mathbf{n}_{b_\omega}, \mathbf{n}_v\right)$. We assume that the additive noise $\mathbf{n}_a$, $\mathbf{n}_\omega$, $\mathbf{n}_{b_a}$, $\mathbf{n}_{b_\omega}$, and $\mathbf{n}_v$ are modeled as zero-mean, white Gaussian noise.

The Jacobian matrix is propagated as

$$\mathbf{J}_{b_{\tau+1}}^{b_k} = (\mathbf{I} + \mathbf{F}_\tau \Delta t) \, \mathbf{J}_{b_\tau}^{b_k}. \tag{10}$$

The initial Jacobian matrix is $\mathbf{J}_{b_k} = \mathbf{I}$.

4. Multi-sensor-fusion factor graph framework

This section describes the framework of the proposed factor graph for integrating onboard sensors with raw GNSS data to estimate the vehicle's state. The structure of the factor graph is illustrated in figure 4. The IMU/Dynamics factor is represented by yellow rectangles, and the clock drift factor is represented by blue rectangles. The noise associated with these factors is modeled using Gaussian distributions. Since this is a commonly adopted model, we will not describe in detail. The purple rectangles represent the pseudorange factor. To address the challenges posed by the time-varying and non-Gaussian characteristics of pseudorange noise in multi-sensor fusion, we estimate the noise model for pseudorange online. Additionally, pseudorange noise is characterized using a GMM. In the following, we provide a detailed discussion of each factor and the online estimation algorithm for pseudorange noise model.
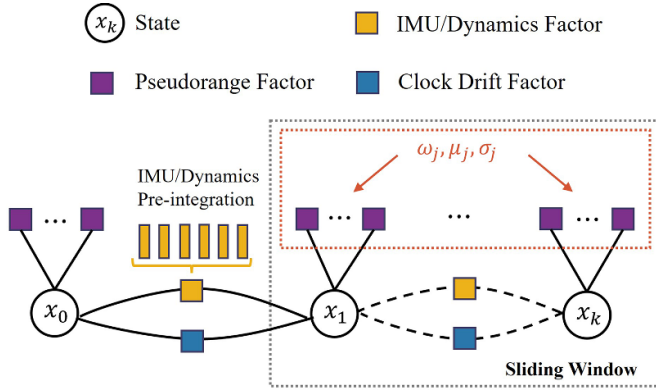
Figure 4. Illustration of factor graph for the proposed GNSS/Onboard sensors integration with GMM.

Our proposed GNSS/Onboard sensors integration system performs a sliding window optimization and the state vector can be summarized as

$$\boldsymbol{\chi} = [\boldsymbol{x}_0, \boldsymbol{x}_1, \ldots, \boldsymbol{x}_k, \ldots, \boldsymbol{x}_L]$$

$$\boldsymbol{x}_k = \left[\mathbf{p}_{b_k}^n, \mathbf{v}_{b_k}^n, \mathbf{q}_{b_k}^n, \mathbf{b}_{a_k}^b, \mathbf{b}_{\omega_k}^b, \delta t_i, \dot{\delta} t_i \right], k \in [0, L] \qquad (11)$$

where $\boldsymbol{\chi}$ stands for the states set in the sliding window and L is the window size. $\boldsymbol{x}_k$ represents the state in time t_k, which includes eighteen variables: the position $\mathbf{p}_b^n$, velocity $\mathbf{v}_b^n$, orientation $\mathbf{q}_b^n$, accelerometer bias $\mathbf{b}_a^b$, gyroscope bias $\mathbf{b}_\omega^b$, receiver clock bias δt, and receiver clock drifting rate $\dot{\delta} t$.

4.1. Graph optimization

The factor graph we proposed includes IMU/Dynamics constraints and GNSS-related constraints. The error function of the proposed method can be formulated as

$$\boldsymbol{\chi}^* = \arg\min_{\boldsymbol{x}} \left\{ \|\mathbf{r}_{\mathrm{P}}(\boldsymbol{\chi})\|^2 + \sum_{k=1}^{L} \left\| \mathbf{r}_{\mathrm{ID}} \left(\widetilde{\mathbf{Z}}_{b_{k+1}}^{b_k}, \boldsymbol{\chi} \right) \right\|_{\sum_{\mathrm{ID}}}^2 \right.$$
$$\left. + \sum_{k=1}^{L} \left\| \mathbf{r}_{\mathrm{C}} \left(\widetilde{\mathbf{Z}}_{b_{k+1}}^{b_k}, \boldsymbol{\chi} \right) \right\|_{\sum_{\mathrm{C}}}^2 + \sum_{k=1}^{L} \left\| \mathbf{r}_{\mathrm{pr}} \left(\widetilde{\mathbf{Z}}_{r_k, s_j}, \boldsymbol{\chi} \right) \right\|_{\mathrm{GMM}}^2 \right\} \qquad (12)$$

where $\mathbf{r}_{\mathrm{P}}(\boldsymbol{\chi})$ stands for the prior information obtained from marginalization. $\mathbf{r}_{\mathrm{ID}}(\widetilde{\mathbf{Z}}_{b_{k+1}}^{b_k}, \boldsymbol{\chi})$, $\mathbf{r}_{\mathrm{C}}(\widetilde{\mathbf{Z}}_{b_{k+1}}^{b_k}, \boldsymbol{\chi})$, and $\mathbf{r}_{\mathrm{pr}}(\widetilde{\mathbf{Z}}_{r_k, s_j}, \boldsymbol{\chi})$ represent IMU/Dynamics, clock drift, and pseudorange residuals, respectively. $\sum_{ID}$ and $\sum_C$ represent the covariance matrices of the IMU/Dynamics pre-integration and clock drift factor, which are set based on the the Gaussian assumption. The noise of pseudorange factor is modeled by GMM, whose parameters are set via the estimation results from EM algorithm, which will be described in section 4.4 in detail. To address the non-linear optimization problem, we employ the Levenberg-Marquardt algorithm in Ceres Solver [32].The specific models of above factors are given as follows.

4.2. IMU/Dynamics factor

In the time interval $[t_k, t_{k+1}]$, the residual that relates the system states and pre-integrated IMU/Dynamics

measurements calculated from section 3.3 can be formulated as

$$\mathbf{r}_{\mathrm{ID}} \left(\widetilde{\mathbf{Z}}_{b_{k+1}}^{b_k}, \boldsymbol{\chi} \right) = \begin{bmatrix} \delta \boldsymbol{\alpha}_{b_{k+1}}^{b_k} \\ \delta \boldsymbol{\beta}_{b_{k+1}}^{b_k} \\ \delta \boldsymbol{\theta}_{b_{k+1}}^{b_k} \\ \delta \boldsymbol{b}_{a_{k+1}} \\ \delta \boldsymbol{b}_{\omega_{k+1}} \\ \delta \boldsymbol{\eta}_{b_{k+1}}^{b_k} \end{bmatrix}$$

$$= \begin{bmatrix} \mathbf{R}_n^{b_k} \left(\mathbf{p}_{b_{k+1}}^n - \mathbf{p}_{b_k}^n + \frac{1}{2} \mathbf{g}^n \Delta t_k^2 - \mathbf{v}_{b_k}^n \Delta t_k \right) - \boldsymbol{\alpha}_{b_{k+1}}^{b_k} \\ \mathbf{R}_n^{b_k} \left(\mathbf{v}_{b_{k+1}}^n + \mathbf{g}^n \Delta t_k - \mathbf{v}_{b_k}^n \right) - \boldsymbol{\beta}_{b_{k+1}}^{b_k} \\ 2 \left[\mathbf{q}_{b_k}^{n^{-1}} \otimes \mathbf{q}_{b_{k+1}}^n \otimes \left(\boldsymbol{\gamma}_{b_{k+1}}^{b_k} \right)^{-1} \right]_{xyz} \\ \boldsymbol{b}_{a_{k+1}} - \boldsymbol{b}_{a_k} \\ \boldsymbol{b}_{\omega_{k+1}} - \boldsymbol{b}_{\omega_k} \\ \mathbf{R}_n^{b_k} \left(\mathbf{p}_{b_{k+1}}^n - \mathbf{p}_{b_k}^n \right) - \boldsymbol{\eta}_{b_{k+1}}^{b_k} \end{bmatrix} \qquad (13)$$

where $\mathbf{g}^n$ represents the gravity vector in the ENU frame. $\delta \boldsymbol{\theta}_{b_{k+1}}^{b_k}$ is the rotation error represented by euler angle, and $[\cdot]_{xyz}$ represents the imaginary part of the quaternion.

4.3. GNSS factor

4.3.1. Pseudorange factor. GNSS consists of four independently operated satellite systems: GPS, GLONASS, Galileo, and Beidou. Because the clock error of each satellite system is different, it should be considered in the application of multi-satellite system. Therefore, to reduce the number of states, only the GPS satellite system is used in this paper. The GNSS receiver can obtain satellite ephemeris and pseudorange measurements. Consider that, at time t_k, the navigation satellite s_j is locked. The position of satellite s_j ($\mathbf{p}_{s_j, k}^e = \begin{bmatrix} X_{s_j, k}^e & Y_{s_j, k}^e & Z_{s_j, k}^e \end{bmatrix}$) can be calculated through ephemeris measurements. The geometric distance between the receiver and the satellite is calculated by multiplying the speed of light *clight* with the time-of-flight of a radio signal. However, it will be affected by various errors that appear during the signal propagation, which include atmospheric delay $\delta \rho_{kn, k}$, ionospheric delay $\delta \rho_{kp, k}$, receiver clock error δt_k, and satellite clock error $\delta t_{s_j, k}$. So the range measurements obtained from the GNSS receiver are called 'pseudorange'.

In the above error terms that affect the accuracy of the pseudorange, receiver clock error δt_k is the maximum component. δt_k is the difference between the receiver clock and the GNSS reference clock. It may vary over time, so we must estimate it along with the position of the receiver. Other errors such as satellite clock error $\delta t_{s_j, k}$, atmospheric delay $\delta \rho_{kn, k}$, and ionospheric delay $\delta \rho_{kp, k}$ can be calculated based on ephemeris measurements [33]. δt_k and $\delta t_{s_j, k}$ are expressed in units of *m*. At the same time, the Sagnac effect $\delta_{s_j, k}^{sag}$ caused by Earth's rotation should be considered as follows [33]

$$\delta_{s_j, k}^{sag} = \frac{\omega_{\mathrm{earth}}}{\mathrm{clight}} \left(X_{s_j, k}^e Y_{r_k}^e - Y_{s_j, k}^e X_{r_k}^e \right). \qquad (14)$$

Based on the errors analysed above, the pseudorange measurement can be modeled as

$$\rho_{k,j} = \left\| \mathbf{p}_{s_j,k}^e - \mathbf{p}_{r_k}^e \right\| + \delta t_k - \delta t_{s_j,k} + \delta \rho_{kn,k} + \delta \rho_{kp,k} + \delta_{s_j,k}^{sag} \tag{15}$$

where ω_{earth} is Earth's rotation rate. $\mathbf{p}_{r_k}^e = \begin{bmatrix} X_{r_k}^e & Y_{r_k}^e & Z_{r_k}^e \end{bmatrix}$ represents the position of the receiver's antenna in ECEF frame. The estimated state $\mathbf{p}_{b_k}^n = \begin{bmatrix} X_{b_k}^n & Y_{b_k}^n & Z_{b_k}^n \end{bmatrix}$ in this paper is the position of vehicle in the ENU frame and specifically it refers to the installation position of the IMU on the vehicle. In order to get $\mathbf{p}_{r_k}^e$, the transformation between ENU frame and ECEF frame is required first. Then the arm $\boldsymbol{l}_r^b$ between the GNSS antenna and the IMU also requires consideration. Therefore, considering that at time t_k, the navigation satellite s_j is observed. The residual that relates the system states and pseudorange measurements can be formulated as

$$\begin{aligned} \mathbf{r}_{pr} \left(\widetilde{\mathbf{Z}}_{r_k,s_j}, \boldsymbol{\chi} \right) &= \left\| \mathbf{p}_{s_j,k}^e - \mathbf{p}_{r_k}^e \right\| + \delta t_k - \delta t_{s_j,k} + \delta \rho_{kn,k} \\ &\quad + \delta \rho_{kp,k} + \delta_{s_j,k}^{sag} - Z_{\rho_{k,j}} \\ \mathbf{p}_{r_k}^e &= \mathbf{T}_n^e \left(\mathbf{p}_{b_k}^n + \mathbf{R}_{b_k}^n \boldsymbol{l}_r^b \right) \end{aligned} \tag{16}$$

where $\mathbf{T}_n^e$ is the transformation matrix between ECEF frame and ENU frame. In this paper, it is set as a constant and calculated from the ECEF coordinates of the origin.

4.3.2. Clock drift factor.

The receiver clock error is not a constant. It often drifts at a certain rate. We model it using the constant clock error drift model [33], which approximates the linear frequency drift of the receiver clock source and allows for random walk of this drift.

$$\mathbf{r}_C \left(\widetilde{\mathbf{Z}}_{b_{k+1}}^{b_k}, \boldsymbol{\chi} \right) = \begin{bmatrix} \delta t_k - \dot{\delta t}_k \triangle t \\ \dot{\delta t}_k \end{bmatrix} - \begin{bmatrix} \delta t_{k+1} \\ \dot{\delta t}_{k+1} \end{bmatrix}. \tag{17}$$

4.4. Pseudorange noise model estimation

Compared to the relative constraints provided by other factors, pseudorange factors provide absolute constraints on the state. Therefore, the quality of pseudorange measurements greatly affects the estimation accuracy. As is well-known, the quality of pseudorange measurements is mainly influenced by external environments. In the course of our research, we found that the noise of pseudorange shows time-varying characteristics in real-world comprehensive environments. In challenging scenarios such as urban canyons, tunnels, and wooded areas, it might exhibit non-Gaussian characteristics. Because the noise parameters are unknown, the above characteristics pose challenges in fusing pseudorange information in a factor graph. To tackle this issue, we estimate the noise model for pseudorange online and adopt GMM instead of the common Gaussian model to represent the pseudorange noise. We use the EM [26] algorithm to estimate the GMM-based noise model online. GMM can be expressed as follows

$$\mathbf{P} \left(\boldsymbol{z}_i \mid \boldsymbol{x}_i \right) \propto \sum_j \omega_j \cdot \lambda \left(\mu_j, \sigma_j^2 \right). \tag{18}$$

For a GMM composed of N Gaussian components, the conditional probability can be expressed as

$$\mathbf{P} \left(\boldsymbol{z}_i \mid \boldsymbol{x}_i \right) \propto \sum_{j=1}^{N} c_j \cdot \exp \left(-\tfrac{1}{2} \left\| (e_i - \mu_j) \right\|_{\sum_j}^2 \right) \tag{19}$$

where

$$c_j = \omega_j \cdot \det \left(\sum_j{}^{-\frac{1}{2}} \right)$$

where ω_j is the weight of the j Gaussian component. μ_j and σ_j^2 represent the mean and variance of the Gaussian component, respectively. When applying GMM to the factor graph, Summixture [29] has better performance compared with Maxmixture [28]. It can be expressed as follows

$$\boldsymbol{x}^* = \arg\min_{\boldsymbol{x}} \sum_i \left\| \sqrt{ -\ln \left(\frac{ \sum_{j=1}^{N} c_j \cdot \exp \left(-\tfrac{1}{2} \left\| (e_i - \mu_j) \right\|_{\sum_j}^2 \right) }{ \gamma_s } \right) } \right\|^2 \tag{20}$$

$$\gamma_s \geqslant \max_i \left(\mathbf{P} \left(\boldsymbol{z}_i \mid \boldsymbol{x}_i \right) \right)$$

where γ_s is a normalized constant to keep the negative log-likelihood positive [29]. In this paper, we set $\gamma_s = \sum_j c_j$. Equation (20) is the complete form of the cost function we constructed by using the pseudorange measurement in section 4.1.

For the problem of unknown noise parameters, we use EM-based online estimation algorithm to avoid a lot of parameter tuning work. The GMM parameter $\boldsymbol{\theta}$ used in equation (20) is estimated by iteratively alternating between the E-step and the M-step based on the residual sequence $\boldsymbol{o}$. Based on the pseudorange residual sequence within a sliding window calculated by equation (16), the E-step estimates the hidden variable $\boldsymbol{H}$. α_{fj} represents the probability of e_f belongs to the j Gaussian component. Then the M-step updates the noise parameters based on the hidden variables. The basic flow of EM algorithm can be found in [26]. The estimated GMM parameters are then applied in the factor graph optimization in equation (12) to achieve adaptive fusion.

$$\begin{cases} \boldsymbol{o} = \{e_1, e_2, \ldots, e_f, \ldots, e_M\} \\ \boldsymbol{H} = \{\alpha_{fj}\}_{f=1,\ldots M, j=1,\ldots N} \\ \boldsymbol{\theta} = \left\{ \omega_j, \mu_j, \sum_j{}^{-\frac{1}{2}} \right\}_{j=1,\ldots N}. \end{cases} \tag{21}$$

The difference between the research work in [26] and our proposed method is our proposed method aims for improving the accuracy of onboard sensor-based positioning. Due to the novel IMU/Dynamics factor which we present by consideration of vehicle dynamics, our method is superior to the method [26]. In addition, the residual accuracy used in the EM algorithm is also improved, it will make the noise parameter estimation of pseudorange measurement more accurate.

5. Experimental validation

In this section, the experimental platform as well as experimental results and discussion are presented.
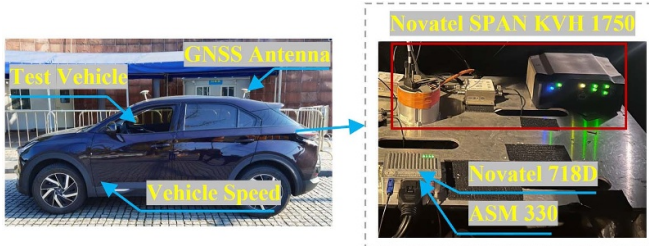
Figure 5. Experimental platform: the left is the experimental vehicle, and the right is the sensor configuration in the trunk.

Table 1. Specifications of sensors.

Sensor	Parameter	Value
Gyroscope	Bias stability	$3°/\mathrm{h}$
	Angular random walk	$0.21°/\sqrt{\mathrm{h}}$
Accelerometer	Bias stability	$80\,\mathrm{mg}$
	Velocity random walk	/
GNSS recevier	Position accuracy	RTK $1\,\mathrm{cm}+1\,\mathrm{ppm}$ RMS
	Velocity accuracy	$<0.03\,\mathrm{m\,s^{-1}}$ RMS
KVH 1750	Position accuracy	RTK $1\,\mathrm{cm}+1\,\mathrm{ppm}$ RMS
	Velocity accuracy	$0.01\,\mathrm{m\,s^{-1}}$ RMS
	Pitch and roll accuracy	$0.015°$
	Heading accuracy	$0.04°(2\,\mathrm{m}$ baseline)
Wheel speed	Position accuracy	$0.01 \times$ Distance

5.1. Experimental set-up

To validate the proposed algorithm, comprehensive experiments are conducted on the vehicle platform as shown in figure 5 consisting of urban canyons, tunnels, and wooded areas scenarios. During the experiments, the steering wheel angle and wheel speed data are acquired from the controller area network bus interface of the vehicle. Raw multi-frequency GNSS data is collected from the Novatel 718D GNSS receiver at 1 Hz. The automotive-grade IMU used is the ASM330LHH from ST company, which provides acceleration and angular velocity measurements along three axes at 100 Hz. The GNSS receiver and IMU are integrated into a microchip controller. The ground truth for positioning is obtained from the NovAtel SPAN-KVH 1750, a high precision GNSS/INS integrated system that consists of a GNSS receiver and fiber-optic gyroscopes. Detailed specifications of the sensors can be found in table 1. All data are hardware synchronized.

In the factor graph optimization of our algorithm, the length of sliding window is set to 60s for balancing the runtime and accuracy. Additionally, from the histogram of the pseudorange residuals in figure 7, we can observe two noticeable peaks in the distribution. Thus at least two Gaussian components are required to describe the pseudorange noise distribution shown in figure 7. Therefore, we set the number of Gaussian components in the GMM to 2, which is used in section 4.4. Table 2 summarizes the remaining parameters that are used in our proposed algorithm.

Table 2. Noise properties

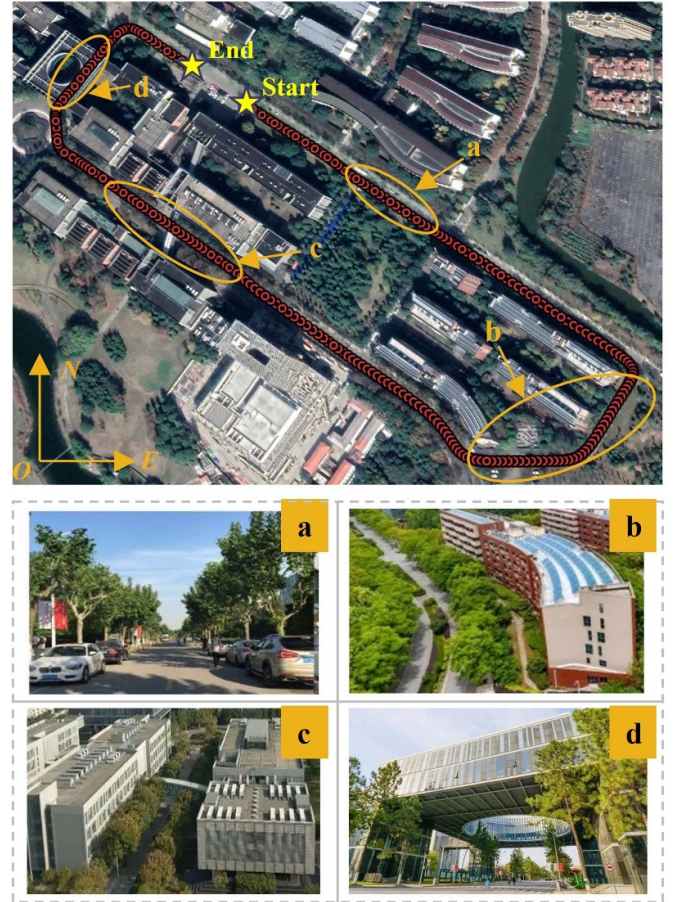| Factor	Parameter	Value
Pseudorange	Inital value of GMM	$\begin{cases} \mu_j &= 0 \\ \sigma_j &= 10^j \\ \omega_j &= \frac{1}{N} \end{cases}$
Clock drift	Covariance	$\begin{pmatrix} 0.05\,\mathrm{m} \\ 0.01\,\mathrm{m\,s^{-1}} \end{pmatrix}$

Figure 6. Trajectory of the vehicle in the road experiments. The challenging scenarios include wooded areas (a) and (b), urban canyons (c), and tunnels (d).

In figure 6, the comprehensive experiment consisting of various typical GNSS degradation scenarios (wooded areas (a) and (b), urban canyons(c), and tunnels(d)) is conducted at Tongji University, Jiading campus to verify the effectiveness of the proposed algorithm. The experimental trajectory is illustrated in figure 6, in which the red line represents the vehicle trajectory and the yellow star indicates the starting and ending point of the route. The experiment includes scenarios such as urban canyons, tunnels and wooded areas, which have been marked with yellow circles in figure 6.

To verify the performance of the proposed method, we compare five different algorithms: RTKLIB, libRSF, GNSS/O GMM, GNSS/IO, and GNSS/IO GMM. RTKLIB represents a pseudorange-based single point positioning algorithm
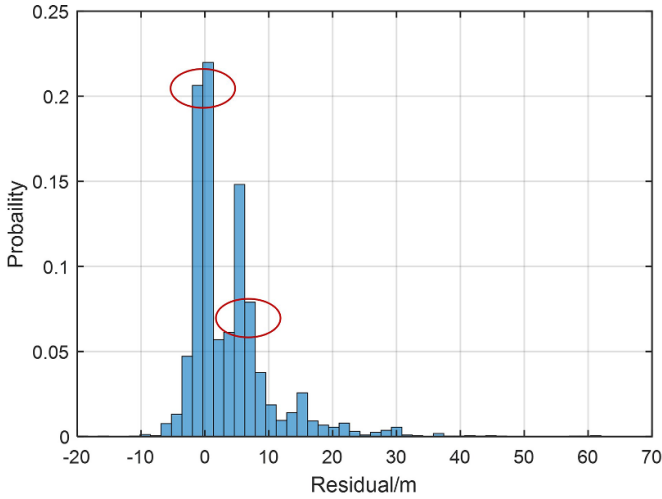
Figure 7. The histogram of the pseudorange residuals during the experiment(The residuals are calculated using the ground truth of position).

Figure 8. The distribution of satellites and the pseudorange residuals of each satellite. In our experiment, only eight satellites are observed at most. The image on the left shows the distribution of satellites observed at one time.

implemented using the weighted least squares method [33]. Since only pseudorange measurements are used, the position accuracy of this algorithm reflects the quality of the pseudorange. Therefore, in the following discussion, we evaluate the robustness of other algorithms based on their position accuracy relative to RTKLIB. libRSF [26] serves as the baseline algorithm in this paper, which tightly integrates the pseudorange and the wheel speed in a factor graph. The pseudorange noise is modeled by the GMM and estimated online by the EM. The wheel speed constraint is based on the assumption of vehicle planar motion. GNSS/O GMM, GNSS/IO and GNSS/IO GMM are different variations of the algorithm proposed in this paper. Among them, GNSS/O GMM only integrates the dynamics pre-integration proposed in this paper with the pseudorange factor. In this approach, the pseudorange noise is also modeled using GMM and estimated online. GNSS/IO GMM is the complete version of our algorithm, which further incorporates the IMU pre-integration to construct the IMU/Dynamics factor on the basis of GNSS/O GMM. The difference between GNSS/IO and GNSS/IO GMM lies in the modeling of pseudorange noise. GNSS/IO adopts Gaussian modeling, with the variance calculated based on signal-to-noise ratio, satellite elevation and other information [33]. The ground truth is expressed as GT.

5.2. Validation of pseudorange noise characteristics

Figure 7 shows the histogram of pseudorange residuals obtained from all observed satellites from the GNSS receiver during the experiment. We can observe two peaks in the distribution, along with a significant tail on the right side. This confirms that the pseudorange noise violates the Gaussian distribution in challenging scenarios such as urban canyons, tunnels, and wooded areas. At least two Gaussian components are required to describe the distribution of the pseudorange noise indicated in figure 7. In order to better analyze the reasons for this phenomenon, we present the pseudorange residual-time
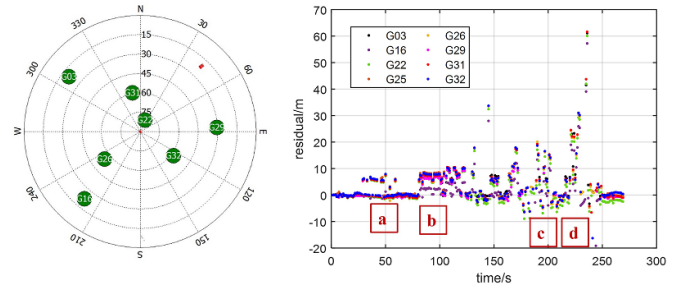
graph for individual satellite, as shown in figure 8. In the initial period, as the vehicle drives in the open sky area, the pseudorange residual for each satellite remains relatively stable and close to zero. However, as the vehicle enters wooded areas (depicted in parts (a) and (b) of figure 8), the pseudorange residuals exhibit the overall deviation, which becomes more obvious in scene (b) with denser tree coverage. In scenes (c) and (d), more severe and irregular data jumps occur due to the influence of the tall buildings on both sides. All of these lead to the non-Gaussian distribution of the pseudorange noise.

It can be seen from figure 8 that the pseudorange noise exhibits time-varying characteristics across different scenarios. Moreover, the noise parameters are unknown. Therefore, in order to make better use of pseudorange data in sensor fusion processes, online estimation of its noise parameter becomes crucial. As can be seen from the statistical results of position accuracy (table 3), the GNSS/IO GMM algorithm which employs GMM for modeling pseudorange noise and performs online estimation of noise parameters, outperforms the GNSS/IO algorithm. The mean absolute error (MAE) of position is reduced by nearly 2 m, and the position accuracy is improved by 36.6% in terms of root mean square error (RMSE). These results validate the effectiveness of employing GMM to describe the pseudorange noise and using the EM algorithm for online estimation of GMM parameters.

5.3. Positioning accuracy evaluation experiment

The comparison of horizontal position errors is shown in figure 9. It can be seen that the proposed GNSS/IO GMM algorithm achieves the best performance. To quantitatively analyze the position errors, MAE, RMSE, and Maximum error are employed as performance metrics. The statistical results are shown in table 3. In terms of RMSE, there is a 39.4% improvement compared to the baseline algorithm libRSF. Further analysis is conducted to evaluate the positioning performance in different scenarios. It can be seen from parts (a) and (b) of figure 9 that the position error of RTKLIB reaches around 8 *m* in the wooded scenes (a) and (b), which relies only on pseudorange position. It is consistent with the increase of pseudorange error discussed in section 5.2. In the urban canyon scenes (c) and (d), the pseudorange errors escalate and accompanies by occlusion that limits satellite observations.

Table 3. Position errors of the evaluated methods.

Methods	RTKLIB	libRSF	Our methods		
			GNSS/IO	GNSS/O GMM	GNSS/IO GMM
MAE(m)	20.237	3.017	4.326	2.643	**2.298**
RMSE(m)	28.548	3.833	4.453	2.821	**2.324**
Maximum(m)	110.699	13.214	5.804	6.263	**3.431**
Improvement*	**91.8%**	**39.4%**	**47.8%**	**17.6%**	/

Improvement* means the percentage improvement of proposed method compared to the listed methods in RMSE.
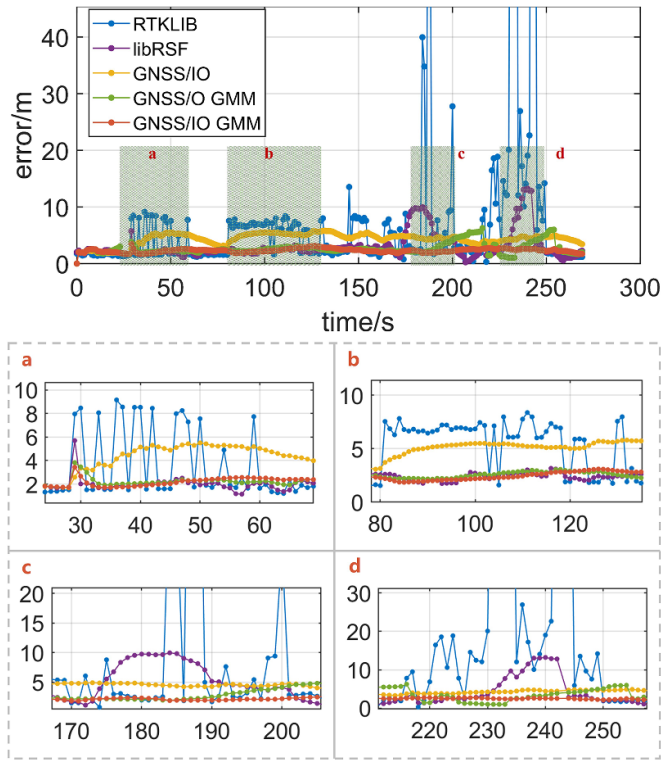
Figure 9. Positioning errors of the tested methods.

Figure 10. The number of satellites observed.

It can be seen from figure 10 that there are even cases with fewer than four satellites observed. It will lead to the divergence of RTKLIB with errors reaching tens or even hundreds of meters (Note that for better visualization of the errors for each method, the part with large errors of RTKLIB is truncated in figure 9). Consequently, pseudorange-based position encounters significant challenges in such scenarios. Compared with RTKLIB, libRSF has shown improvement, especially in scenes (a) and (b). However, in the more challenging scenes (c) and (d), error drift still occurs. In contrast, our proposed algorithm GNSS/IO GMM consistently maintains good position accuracy across all scenarios without being affected by GNSS outliers. This verifies the robustness of our algorithm.

5.3.1. Influence of dynamics pre-integration. In order to validate the effectiveness of our proposed dynamics pre-integration model, we compare and analyze the performance of libRSF and GNSS/O GMM algorithms. As shown in
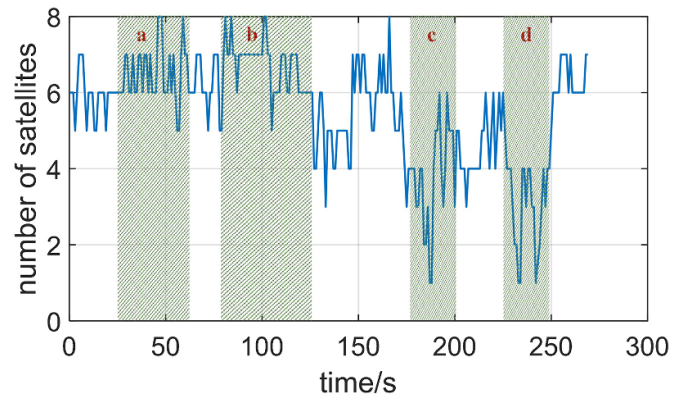
table 3, our algorithm GNSS/O GMM demonstrates a significant improvement in position accuracy, with a 26.4% increase in RMSE and a reduction of 0.374 m in MAE. It can be seen from figure 9 that both algorithms achieve similar position accuracy in the wooded scenes (a) and (b). However, in the more challenging scenes (c) and (d), the GNSS/O GMM algorithm exhibits significant improvements. On the other hand, libRSF obviously follows the fluctuations of the pseudorange-based positioning in RTKLIB, which indicating its inability to effectively mitigate the impact of GNSS outliers. In contrast, GNSS/O GMM performs well in this regard. The trajectories presented in figure 11 further validate these observations. In scenes (c) and (d), the trajectory of GNSS/O GMM is smoother and demonstrates higher accuracy in heading angle compared to libRSF. This confirms the effectiveness of adding more accurate 3D attitude constraints. It shows that the dynamics pre-integration model proposed by us has better performance.

In order to further analyze the significant improvement of our proposed algorithm GNSS/O GMM compared to the baseline algorithm libRSF in scenes (c) and (d), we separately plot the histogram of pseudorange residuals in these scenes as shown in figure 12. It is evident that the pseudorange error is not consistent with the zero-mean Gaussian distribution due to many GNSS outliers. Table 4 provides a summary of the estimated GMM parameters in scene (c). We compare the estimation results of GNSS/O GMM and libRSF. It can be seen that GNSS/O GMM is closer to the GT, particularly in terms of the mean value of the component two. The parameters of component two mainly characterizes the outlier measurements, so that enables GNSS/O GMM to effectively mitigate their impact.
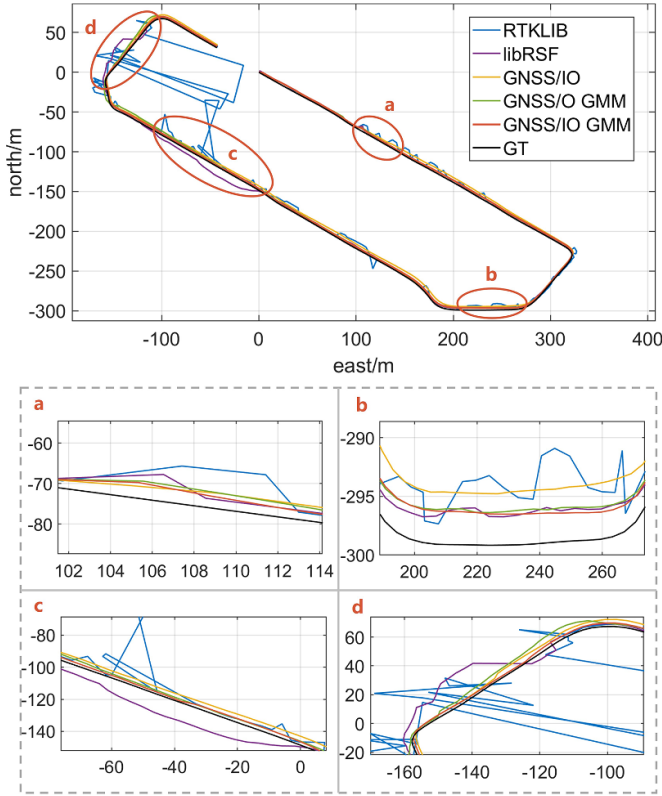
Figure 11. Trajectories of the tested methods.

The situation in scene (d) is similar as shown in table 5. On the one hand, GMM parameter estimation is based on pseudorange residuals. Therefore, more accurate parameter estimation means that the pseudorange residuals calculated by our algorithm are more accurate. From equation (16), we can infer that this improvement is attributed to more accurate position estimation. Hence, it further demonstrates that our dynamics pre-integration model achieves higher accuracy in position prediction. On the other hand, the position accuracy primarily depends on the odometry after suppressing the influence of GNSS outliers. However, odometry is prone to error accumulation. Parts (c) and (d) of figure 9 illustrate that the GNSS/O GMM algorithm exhibits error drift, with the maximum position error occurring in these scenes. This behavior is mainly caused by the accumulation of odometry errors. Consequently, this observation motivates us to further introduce IMU pre-integration, particularly constraints from accelerometer measurements, to establish a more accurate odometry and further improve the position accuracy.

5.3.2. Influence of IMU/Dynamics factor.
On the basis of dynamics pre-integration in GNSS/O GMM, we further introduces IMU pre-integration to construct integrated IMU/Dynamics factor, which is our complete algorithm. Table 3 demonstrates that integrating the IMU pre-integration leads to a 13% improvement in MAE, a 17.6% increase in RMSE, and a reduction of 2.832 m in the Maximum error. This confirms the effectiveness of utilizing low-cost onboard sensor odometry that adopts integrated IMU/Dynamics
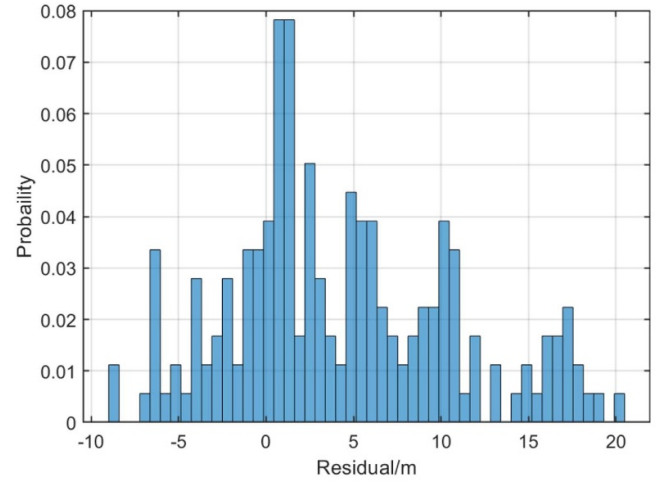
(a) The pseudorange residual histogram of scene (c).
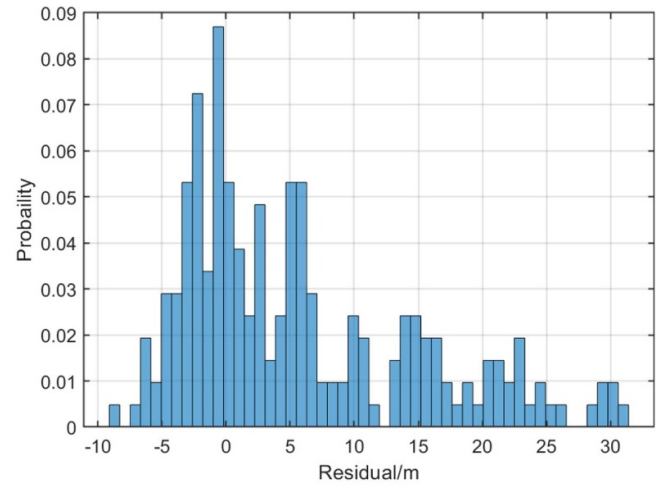
(b) The pseudorange residual histogram of scene (d).

Figure 12. The pseudorange residual histogram of scenes (c) and (d).

Table 4. GMM parameter estimation results in scene (c).

Methods	Component 1 (Mean std weight)	Component 2 (Mean std weight)
GT	(0.697, 3.985, 0.632)	(10.445, 5.123, 0.368)
libRSF	(0.002, 0.251, 0.723)	(1.009, 7.631, 0.277)
GNSS/O GMM	(−0.001, 0.309, 0.868)	**(6.106, 6.003, 0.132)**
GNSS/IO GMM	(−0.647, 1.704, 0.661)	**(9.414, 5.216, 0.339)**

factors to achieve precise state estimation. Examination of tables 4 and 5 reveals that the estimated GMM parameter of GNSS/IO GMM is closer to GT compared to GNSS/O GMM, particularly concerning the mean value of component 2. Consequently, the GNSS/IO GMM algorithm effectively mitigates the impact of GNSS outliers. Moreover, figure 9, specifically in parts (c) and (d), illustrates that GNSS/IO GMM exhibits less error drift compared to GNSS/O GMM in these scenarios. This suggests that the odometry, which relies

Table 5. GMM parameter estimation results in scene (d).

Methods	Component 1 (Mean std weight)	Component 2 (Mean std weight)
GT	(0.159, 3.698, 0.621)	(14.915, 7.94, 0.379)
libRSF	(−0.070, 0.615, 0.716)	(6.484, 5.421, 0.284)
GNSS/O GMM	(−0.004, 0.537, 0.792)	**(8.441, 4.929, 0.208)**
GNSS/IO GMM	(−0.012, 0.747, 0.84)	**(10.029, 4.179, 0.16)**

Table 6. Attitude and velocity errors of the evaluated methods.

Methods		GNSS/O GMM		GNSS/IO GMM	
		MAE	RMSE	MAE	RMSE
Attitude (deg)	Roll	−4.839	44.29	**0.127**	**0.51**
	Pitch	2.556	7.56	**−0.385**	**0.58**
	Yaw	0.697	3.89	**−0.06**	**0.84**
Velocity (m s^{-1})	Ve	−0.16	3.56	**−0.002**	**0.061**
	Vn	−0.099	2.74	**0.003**	**0.052**
	Vu	**−0.003**	**0.04**	−0.018	0.045

on IMU and vehicle dynamic information, offers improved recursive accuracy. Table 6 presents a summary of the quantitative comparison results for attitude error and velocity error between the two algorithms. It is evident that the integrated IMU/Dynamics factors effectively enhance the estimation accuracy of attitude and velocity. This improvement primarily stems from the inclusion of more precise acceleration measurements.

The experiments above verify the effectiveness of the proposed method in practical application. Our work demonstrates the potential for reliable positioning based on low-cost on-board sensors. It shows that the proposed integrated IMU/Dynamics factors compensate for the shortcomings of relying on the assumption of vehicle plane motion, especially in the GNSS challenging scenarios. Compared to the baseline algorithm libRSF [26], which is based on traditional assumptions of vehicle planar motion, achieving a 39.4% improvement in RMSE in challenging scenarios. In addition, our experimental results visually demonstrate the time-varying non-Gaussian noise characteristics of GNSS signals in common driving scenarios. Benefiting from the accurate odometry we constructed, the estimated noise parameters of pseudorange data are more aligned with the actual noise distribution. So that our positioning results can be free from GNSS outliers.

The developed generic factor graph framework facilitates fusion with other available sensors in ADSs. For example, it can be further combined with carrier phase data for outdoor centimeter-level positioning, and can also be applied to fusion with cameras and LiDAR to improve indoor positioning accuracy.

6. Conclusion

To achieve cost-effective and reliable position, this paper proposes a GNSS/onboard sensors fusion localization framework based on factor graph optimization. The framework that we proposed can effectively integrate onboard sensors to realize the full potential of low-cost onboard sensors for reliable positioning. Utilizing measurements from the WSS, steering wheel angle sensor, and MEMS-IMU, we construct novel integrated IMU/Dynamics factors based on combining the 2D dynamic vehicle model with the 3D kinematic model in the graph, resulting in accurate odometry. Our method exhibits better performance in terms of robustness and accuracy when compared to the existing approaches libRSF [26], which is based on traditional assumptions of vehicle planar motion and ignores vehicle dynamic characteristics. Using the reliable odometry, we achieve accurate online estimates of GNSS noise, which effectively mitigates the issues of position accuracy degradation caused by multipath effects and NLOS reception. The adaptive fusion strategy can be easily extended to the fusion of sensors such as cameras and LiDAR.

Future research will primarily focus on the following areas. Firstly, we find that the window size of EM algorithm significantly affects the accuracy of noise parameter estimation. The window size should be dynamically adjusted to adapt to the environment and track changes in signal quality over time. Secondly, we will introduce additional sensor data such as cameras, LiDAR, and carrier phase to achieve reliable indoor and outdoor positioning.

Data availability statement

All data that support the findings of this study are included within the article (and any supplementary files).

J Zhu *et al*

China Under Grants 51975414, and U19A2069; in part by the Young Elite Scientists Sponsorship Program by China Association for Science and Technology (CAST) Under Grant 2021QNRC001; and in part by the Fundamental Research Funds for the Central Universities.

ORCID iD

Jiaqi Zhu ⬤ https://orcid.org/0009-0004-5638-6325

References

[1] Wang X, Li X, Chang H, Li S, Shen Z and Zhou Y 2023 Give: a tightly coupled rtk-inertial-visual state estimator for robust and precise positioning *IEEE Trans. Instrum. Meas.* **72** 1–15
[2] Li S, Gong K, Liu, C H, Wang Y, Qiao F and Cheng X 2021 Metasaug: meta semantic augmentation for long-tailed visual recognition *Proc. of the IEEE/CVF Conf. on computer vision and pattern recognition* pp 5212–21
[3] Cong P, Zhu X, Qiao F, Ren Y, Peng X, Hou Y, Xu L, Yang R, Manocha D and Ma Y 2022 Stcrowd: a multimodal dataset for pedestrian perception in crowded scenes *Proc. IEEE/CVF Conf on Computer Vision and Pattern Recognition* 19608–17
[4] Li Y *et al* 2020 Toward location-enabled IoT (le-IoT): IoT positioning techniques, error sources and error mitigation *IEEE Internet Things J.* **8** 4035–62
[5] Li Y, He Z, Gao Z, Zhuang Y, Shi C and El-Sheimy N 2018 Toward robust crowdsourcing-based localization: a fingerprinting accuracy indicator enhanced wireless/magnetic/inertial integration approach *IEEE Internet Things J.* **6** 3585–600
[6] Sun R, Fu L, Wang G, Cheng Q, Hsu L-T and Ochieng W Y 2021 Using dual-polarization gps antenna with optimized adaptive neuro-fuzzy inference system to improve single point positioning accuracy in urban canyons *Navigation* **68** 41–60
[7] Hong X, Gan T, Lin M, Chang N, Wang W and Yin Q 2020 A subspace-based spatial and temporal multipath mitigation for multi-antenna gps receiver *2020 IEEE/ION Position, Location and Navigation Symp. (PLANS)* (IEEE) pp 1256–66
[8] Zhang G, Wen W, Xu B and Hsu L-T 2020 Extending shadow matching to tightly-coupled GNSS/ins integration system *IEEE Trans. Veh. Technol.* **69** 4979–91
[9] Wen W, Zhang G and Hsu L-T 2018 Exclusion of GNSS nlos receptions caused by dynamic objects in heavy traffic urban scenarios using real-time 3d point cloud: an approach without 3D maps *2018 IEEE/ION Position, Location and Navigation Symp. (PLANS)* (IEEE) pp 158–65
[10] Beuchert J, Camurri M and Fallon M 2022 Factor graph fusion of raw GNSS sensing with imu and lidar for precise robot localization without a base station (arXiv:2209.14649)
[11] Wen W, Bai X, Kan Y C and Hsu L-T 2019 Tightly coupled GNSS/INS integration via factor graph and aided by fish-eye camera *IEEE Trans. Veh. Technol.* **68** 10651–62
[12] Cao S, Lu X and Shen S 2022 Gvins: tightly coupled GNSS–visual–inertial fusion for smooth and consistent state estimation *IEEE Trans. Robot.* **38** 2004–21
[13] Gong Z, Ying R, Wen F, Qian J and Liu P 2019 Tightly coupled integration of GNSS and vision slam using 10-dof optimization on manifold *IEEE Sens. J.* **19** 12105–17
[14] Chiang K-W, Chang H-W, Li Y-H, Tsai G-J, Tseng C-L, Tien Y-C and Hsu P-C 2019 Assessment for INS/GNSS/odometer/barometer integration in

loosely-coupled and tightly-coupled scheme in a GNSS-degraded environment *IEEE Sens. J.* **20** 3057–69
[15] Gao L, Xiong L, Xia X, Lu Y, Yu Z and Khajepour A 2022 Improved vehicle localization using on-board sensors and vehicle lateral velocity *IEEE Sens. J.* **22** 6818–31
[16] Bai S, Lai J, Lyu P, Cen Y and Ji B 2021 Improved preintegration method for GNSS/IMU/IN-vehicle sensors navigation using graph optimization *IEEE Trans. Veh. Technol.* **70** 11446–57
[17] Lu Y, Xiong L, Xia X, Gao L and Yu Z 2022 Vehicle heading angle and IMU heading mounting angle improvement leveraging GNSS course angle *Proc. Inst. Mech. Eng.* D **237** 2249–61
[18] Tong Q, Peiliang Li, and Shen S 2018 Vins-mono: a robust and versatile monocular visual-inertial state estimator *IEEE Trans. Robotics* **34** 1004–20
[19] Quan M, Piao S, Tan M and Huang S-S 2019 Tightly-coupled monocular visual-odometric slam using wheels and a mems gyroscope *IEEE Access* **7** 97374–89
[20] Liu J, Gao W and Hu Z 2019 Visual-inertial odometry tightly coupled with wheel encoder adopting robust initialization and online extrinsic calibration *2019 IEEE/RSJ Int. Conf. on Intelligent Robots and Systems (IROS)* (IEEE) pp 5391–7
[21] Xiao H, Han Y, Zhao J, Cui J, Xiong L and Yu Z 2021 Lio-vehicle: A tightly-coupled vehicle dynamics extension of lidar inertial odometry *IEEE Robot. Autom. Lett.* **7** 446–53
[22] Xia X, Hashemi E, Xiong L, Khajepour A and Xu N 2021 Autonomous vehicles sideslip angle estimation: single antenna GNSS/IMU fusion with observability analysis *IEEE Internet Things J.* **8** 14845–59
[23] Reuper B, Becker M and Leinen S 2018 Benefits of multi-constellation/multi-frequency GNSS in a tightly coupled GNSS/IMU/odometry integration algorithm *Sensors* **18** 3052
[24] Wen W, Pfeifer T, Bai X and Hsu L-T 2020 Comparison of extended kalman filter and factor graph optimization for GNSS/INS integrated navigation system (arXiv:2004.10572)
[25] Xiong L, Kang R, Zhao J, Zhang P, Xu M, Ju R, Ye C and Feng T 2021 G-vido: a vehicle dynamics and intermittent GNSS-aided visual-inertial state estimator for autonomous driving *IEEE Trans. Intell. Trans. Syst.* **23** 11845–61
[26] Pfeifer T and Protzel P 2019 Expectation-maximization for adaptive mixture models in graph optimization *2019 International Conf. Robotics and Automation (ICRA)* (IEEE) pp 3151–7
[27] Watson R M 2019 *Enabling Robust State Estimation Through Covariance Adaptation* (West Virginia University)
[28] Olson E and Agarwal P 2013 Inference on networks of mixtures for robust robot mapping *Int. J. Robot. Res.* **32** 826–40
[29] Rosen D M, Kaess M and Leonard J J 2013 Robust incremental online inference over sparse factor graphs: Beyond the gaussian case *2013 IEEE Int. Conf. on Robotics and Automation* (IEEE) pp 1025–32
[30] Wen W, Bai X, Hsu L-T and Pfeifer T 2020 Gnss/lidar integration aided by self-adaptive gaussian mixture models in urban scenarios: an approach robust to non-gaussian noise *2020 IEEE/ION Position, Location and Navigation Symp. (PLANS)* (IEEE) pp 647–54
[31] Pfeifer T and Protzel P 2018 Robust sensor fusion with self-tuning mixture models *2018 IEEE/RSJ Int. Conf. on Intelligent Robots and Systems (IROS)* (IEEE) pp 3678–85
[32] Agarwal S and Mierle K 2012 *Ceres Solver: Tutorial & Reference* (Google Inc.) vol 2 p 8
[33] Takasu T and Yasuda A 2009 Development of the low-Cost rtk-gps Receiver With an Open Source Program Package Rtklib *Int. Symp. on GPS/Gnss* vol 1 (International Convention Center Jeju Korea Seogwipo-si) pp 1–6